

Statistical Temperature Coefficient Distribution in Analog RRAM Array: Impact on Neuromorphic System and Mitigation Method

AFFILIATIONS

Heng Xu¹, Yue Sun², Yangyang Zhu², Xiaohu Wang^{2,a)}, Guoxuan Qin^{1,a)}

¹School of Microelectronics, Tianjin University, Tianjin, 300072, PR China

²School of Mechanical Engineering, Dalian University of Technology, Dalian, Liaoning, 116024, PR China

^{a)} Authors to whom correspondence should be addressed: wangxiaohu@dlut.edu.cn and gqin@tju.edu.cn

ABSTRACT

Emerging analog resistive random access memory (RRAM) based on HfO_x is an attractive device for non-von Neumann neuromorphic computing systems. The differences in temperature dependent conductance drift among cells hamper computing accuracy, characterized by the statistical distribution of temperature coefficient($T\alpha$). A compact model was presented in order to investigate the statistical distribution of $T\alpha$ under different resistance states. Based on this model, the physical mechanism of thermal instability of cells with a positive $T\alpha$ was elucidated. Furthermore, this model can also effectively evaluate the impact of conductance distribution of different levels under various temperatures in artificial neural networks (ANN). An approach incorporating the optimized conductance range selection and the current compensation scheme was proposed to reduce the impacts of the distribution of $T\alpha$. The simulation results showed that recognition accuracy was improved from 79.8% to 89.6% for the application of MNIST handwriting digits classification with a two-layer perceptron at 400K after adopting the proposed optimization method.

In recent years, brain inspired neuromorphic computing has demonstrated promising characteristics in terms of computing efficiency and energy consumption compared with conventional Von-Neumann architecture¹. Non-volatile memory represented by resistive random access memory (RRAM) has been extensively studied as synaptic elements in brain-inspired computing, which is mainly used to build a high-speed and low-power neuromorphic computing system²⁻⁷. HfO_x-based RRAM recently has been widely utilized in neuromorphic hardware systems due to its fast switching speed, low power consumption, high reliability, excellent analog switching properties and great compatibility with the mainstream CMOS fabrication process^{8,9}.

However, the calculation accuracy of the neuromorphic computing system based on the memristor is restricted by the non-ideal effect of the memristor, such as endurance and retention degradation, read/write noises, the intrinsic nonlinearity of conductance update¹⁰. Therefore, the impact of device-level and array-level non-ideal effects on the accuracy of neuromorphic computing systems has been widely studied¹¹⁻¹⁴. Meanwhile, the thermal stability of analog or multi-stage RRAM is crucial for neuromorphic terminal devices that work in a wide temperature range. Different from the well-studied binary RRAM used for storage, the resistance of the analog memristor acting as synaptic weights in neuromorphic computing system will overlap significantly with temperature changes and thus which will cause a decrease in inference accuracy¹⁵.

Low-temperature characteristics and the impact of temperature on the reset operation of HfO_x-based RRAM have been studied^{16,17}. Meanwhile, the impact of operating temperature on the read/write reliability has been examined¹⁸. The temperature dependent statistical model has been proposed to predict the transport dependence in the temperature range below 300 K¹⁹. The temperature coefficient(T_α) of resistance is one of the significant indicators for evaluating thermal stability. Opposite to the high resistance state(HRS), the conduction mechanism of HfO_x-based RRAM in the low resistance state(LRS) is considered to be metallic with a positive T_α . The study found that different cells with the same resistance range in the RRAM array will show either positive or negative T_α ²⁰. Therefore, the synaptic weight in the neuromorphic system will further deviate from the initial value with the temperature changes.

In this work, a compact model is proposed to predict the statistical conductance evolution with temperature changes, which can explain the physical origin of the unstable properties of cells with positive T_α . The compact model demonstrates the excellent consistency between experimental data and simulation. Meanwhile, the impact of the statistical distribution of the T_α at the array level on the accuracy of neuromorphic computing systems is effectively evaluated. By selecting the

conductance mapping range and the current compensation scheme, the calculation accuracy of the system can be effectively improved from 79.8% to 89.6% at 400K. This method is invalid when the temperature is lower than 350K. Therefore, maintaining excellent heat dissipation should be given priority to improve the calculation accuracy for neuromorphic systems with a temperature below 350K.

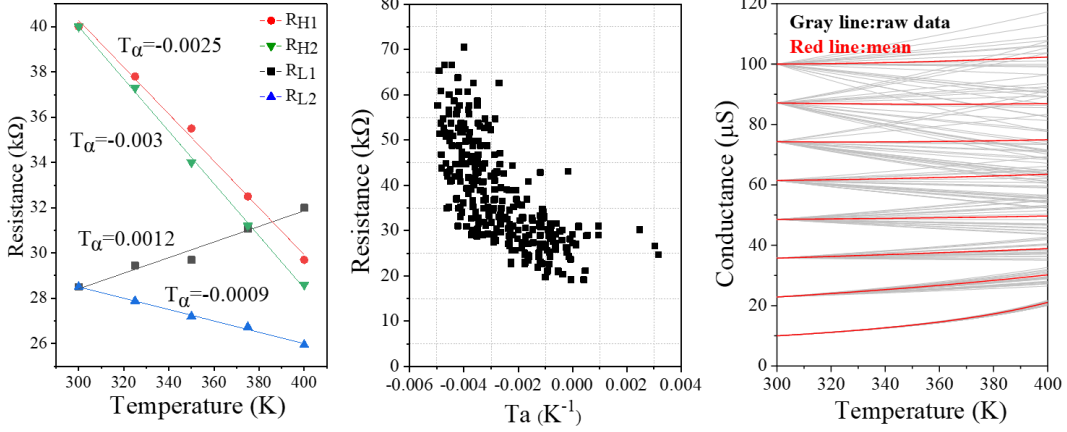


Fig. 1 (a) The temperature dependence of cell resistance with positive and negative T_α . (b) Distribution of T_α versus cell resistance for 1kbit array. (c) The conductance drift of 160 RRAM cells with respect to 8 conductance states as a function of temperature. Every line represents one RRAM cell.

Fig. 1(a) shows temperature dependent measurement results of two different resistance value patterns of HfO_x-based RRAM cells. The resistance of R_{H1} and R_{H2} decreasing with increasing temperature exhibited an explicit doped semiconducting behavior. However, R_L indicated metallic characteristic or semiconducting behavior. The relationship between resistance and temperature can be described by the approximation below²¹,

$$R(T) = R_0[1 + T_\alpha(T - T_0)] \quad (1)$$

where R_0 is resistance at a reference temperature T_0 , and T_α is the temperature coefficient. The statistical distribution results of T_α versus resistance for 1kbit HfO_x-based RRAM array were presented in **Fig. 1(b)**. The conduction mechanism of a minority of low-resistance cells transformed to be metallic. The conductance in RRAM array is simply proportional to the represented weight in neural networks²². Accordingly, the conductance drift was examined intuitively by programming the RRAM cells randomly to eight different conductance, as shown in **Fig. 1(c)**. It is observed that the conductance distribution was very tight at 300K and became wider as temperature increases. The overlap among neighboring conductance occurred at a lower temperature as the conductance increases, which significantly reduced the accuracy of neuromorphic calculations.

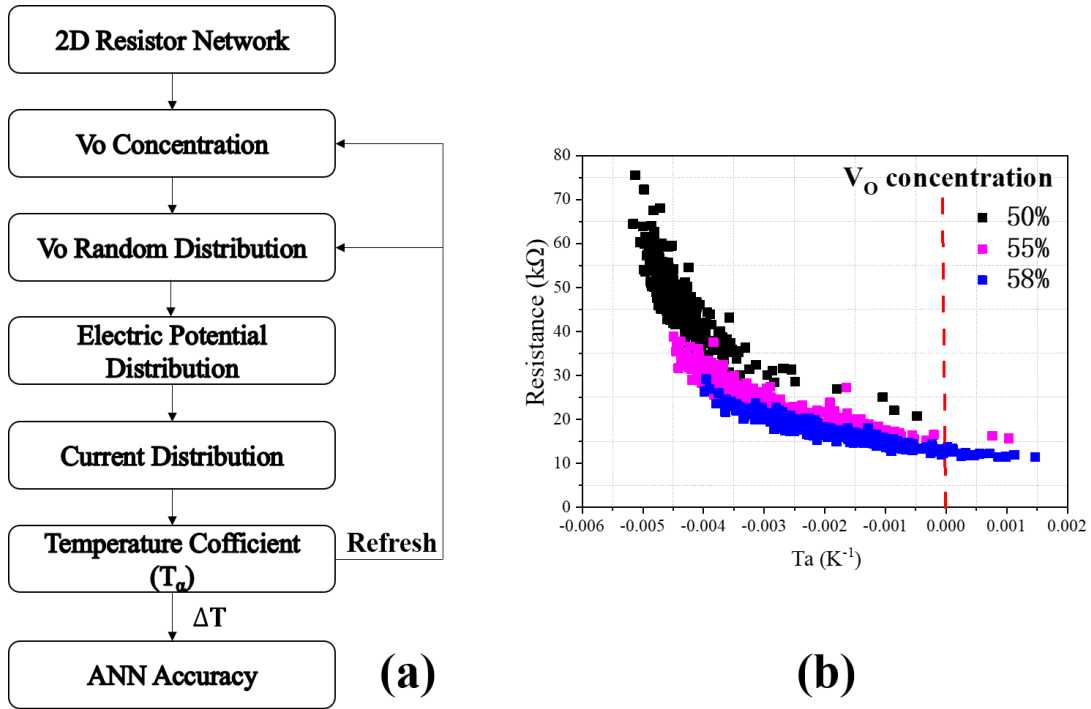


Fig. 2 (a) Simulation flow in this work. (b) Distribution of cell resistance versus T_α of 300 cycles of simulations with oxygen vacancy concentration of 50%, 55%, 58%, respectively.

Different from the conventional strong-filament based RRAM, in multiple-weak-filaments based RRAM, the oxygen vacancies were distributed at a nanoscale region in multiple-weak-filaments based RRAM²³. Therefore, an atomistic simulation method was used to establish a 2D resistance network to simulate the concentration and distribution of oxygen vacancy (V_O) in the filament region. Fig. 2(a) shows the simulation flow. The filament region was equivalent to a stochastic distribution of different concentrations of V_O in a 40×32 matrix, which was proportional to the physical dimensions of an actual device. Kirchhoff's law could solve the electric potential and current distribution in the filament area, and the overall resistance of the network can be further calculated. Similar to Conductive Bridge RAM(CBRAM), filamentary RRAM exhibits negative and positive T_α corresponding to conduction behavior of semiconductors and metals in high and low resistance states, respectively²⁴. Therefore, different adjacent atom connection types in the 2D resistance network where V_O - V_O , V_O - O^{2-} and O^{2-} - O^{2-} were regarded as metallic, semiconductor and insulator resistance, respectively. Meanwhile, distinct adjacent atom connection types have corresponding temperature coefficients according to their different conductivity types.

T_α was calculated using Eq. (1) to fit the overall resistance of the 2D network at different temperatures. Since the distribution of T_α should be correlated with statistical results, the V_O were randomly distributed at a fixed V_O concentration. The above experimental process was repeated 300 times to simulate the differences of cells in the array.

The simulation result of the statistical distribution of the T_α is presented in Fig. 2(b). As the oxygen vacancy concentration increases from 50% to 58%, the T_α of all cells moved to a positive value, and more low-resistance cells obtained positive T_α . A cell with a larger resistance at the same concentration corresponds to a smaller T_α . The simulation result is similar to the experiment data. Under the same resistance state, the lower V_O concentration value in the filament region corresponds to a higher T_α . For the same resistance state cells, the lower V_O concentration in the filament region has a larger T_α . It can thus be suggested that the V_O distribution in low-concentration V_O cells is more concentrated and orderly to form a wider conductive path when the resistance of low-concentration cells is the same as that of the high-concentration cells.

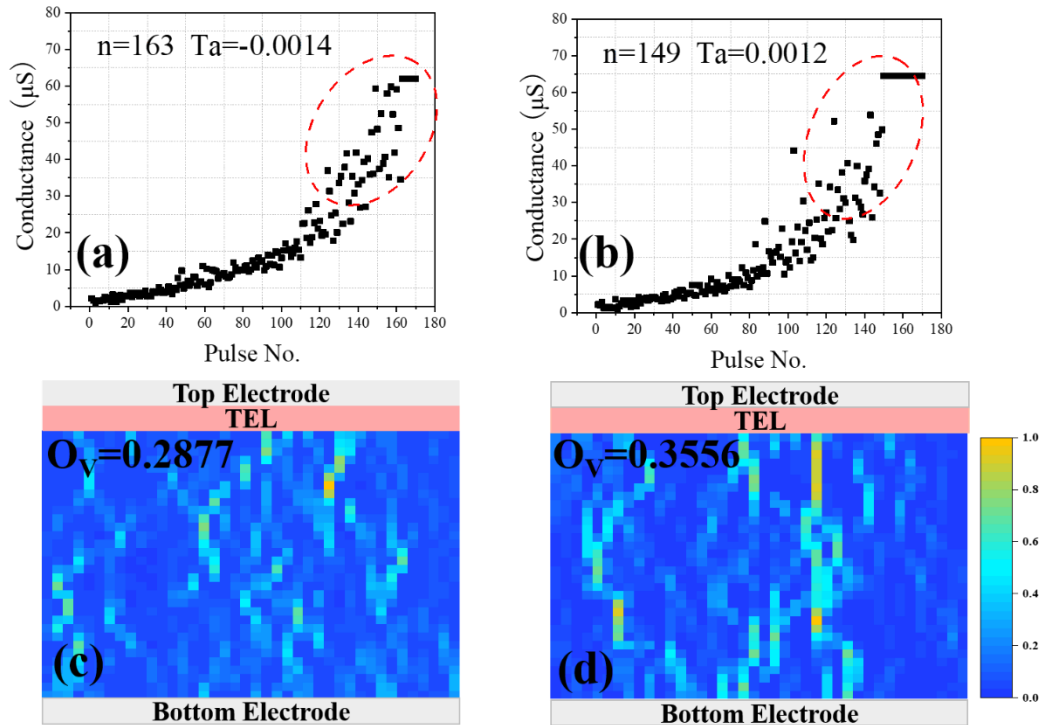


Fig. 3 Simulation results of a SET process of RRAM cells with negative (a) and positive T_α (b) when voltage pulses were applied. n : the number of SET pulses. T_α : The temperature coefficient of the cell when the pulse stopped. Simulated distribution of the normalized current density in the filament region of Hfo_x RRAM with (c) negative T_α and (d) positive T_α .

The analog switch capability of RRAM is essential to realize the high-density weight storage of neuromorphic computing. Hence, simulate the SET process of the RRAM cells using Incremental Step Pulse Program (ISPP) scheme. The cell conductance gradually increased with the application of the SET pulse, which stopped after the device conductance exceeded the target value of $60\mu\text{S}$. Each SET voltage pulse would increase the concentration of V_O in the filament area and redistributes the V_O ²⁵. As shown in Fig. 3(a) and Fig. 3(b), for target conductance value, the SET pulses number of negative T_α cell ($T_\alpha=-0.0014$) is 163, which is significantly larger than that (149) for the positive t cell ($T_\alpha=0.0012$). Meanwhile, compared with a negative T_α cell, the conductance of a positive T_α cell generally had more fluctuations after 120 pulses. Therefore, the analog switching performance of the negative T_α cell is preferable to that of the positive T_α cell. Fig. 3(c) and Fig. 3(d) show the simulated current density distribution of the negative T_α cell and the positive T_α cell. It can be seen that multiple weak CFs are formed due to the percolation effect in the negative T_α cell. In contrast, the apparent conductive path is formed in the positive T_α cell, similar to strong-filament based RRAM. An order parameter of V_O can be used to evaluate the disorder effect of V_O distribution[23], which can be described as

$$O_V = 2N_{V-V}/zC_VN \quad (2)$$

where N_{V-V} is the number of V_O - V_O bond, C_V is V_O concentration, N is the total number of oxygen sites in the filament region, and z is coordinate number of lattice. The dispersity of V_O in the filament region increases as O_V decreases. O_V is lower for the cell with negative T_α than the cell with positive T_α .

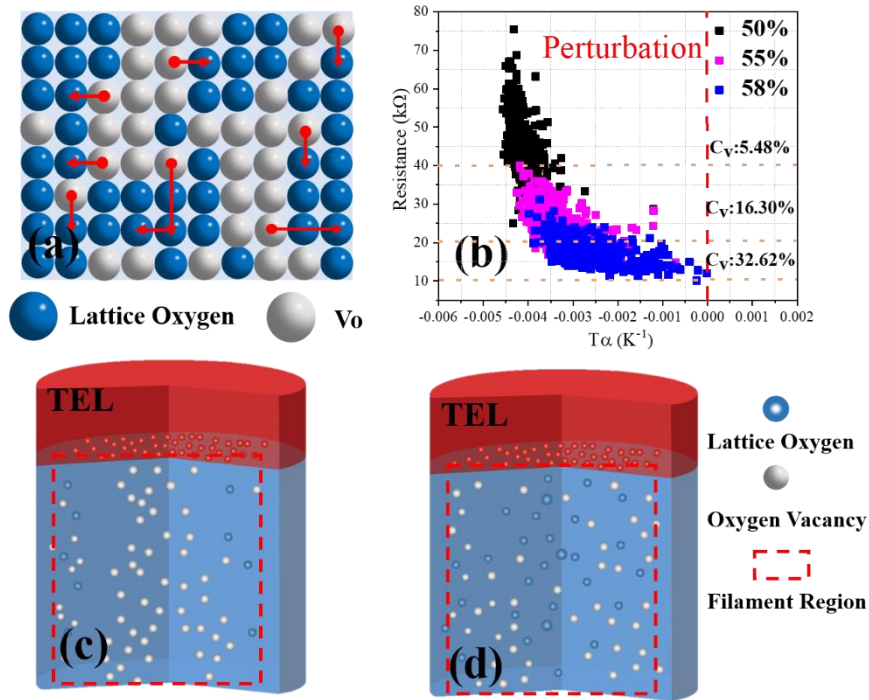


Fig. 4 (a) V_O redistributes when the RRAM cell is perturbed. Most V_O hop at adjacent points, but some V_O can hop to farther points due to repeated reading voltage application or high temperature. (b) Redistribution of cell resistance versus T_α . The coefficient of variation(c_v) was used to evaluate the dispersion of the T_α in different resistance intervals. Schematic views of unstable positive T_α cell (c) and stable negative T_α cell (d) with thermal enhanced layer(TEL).

The retention property of cells with a positive T_α was much worse than that of cells with a negative value²⁰. In order to further reveal the correlation between T_α and retention characteristics, the perturbation process of the RRAM cells was simulated. As shown in **Fig. 4(a)**, after the cells were disturbed, the V_O randomly hops at adjacent lattice sites, or V_O can hop many times where this process was analogy to Brownian Motion. The simulation results of the redistribution of T_α are presented in **Fig. 4(b)**. The T_α of cells at LRS was effectively limited to values below zero. These simulations can confirm that the strong-like filament formed in the filament region is unstable. The V_O distribution in the filamentous region tended to be disordered and scattered. Therefore, repeated write-verify and heating after the programming of the RRAM can reduce the probability of cells with positive T_α .

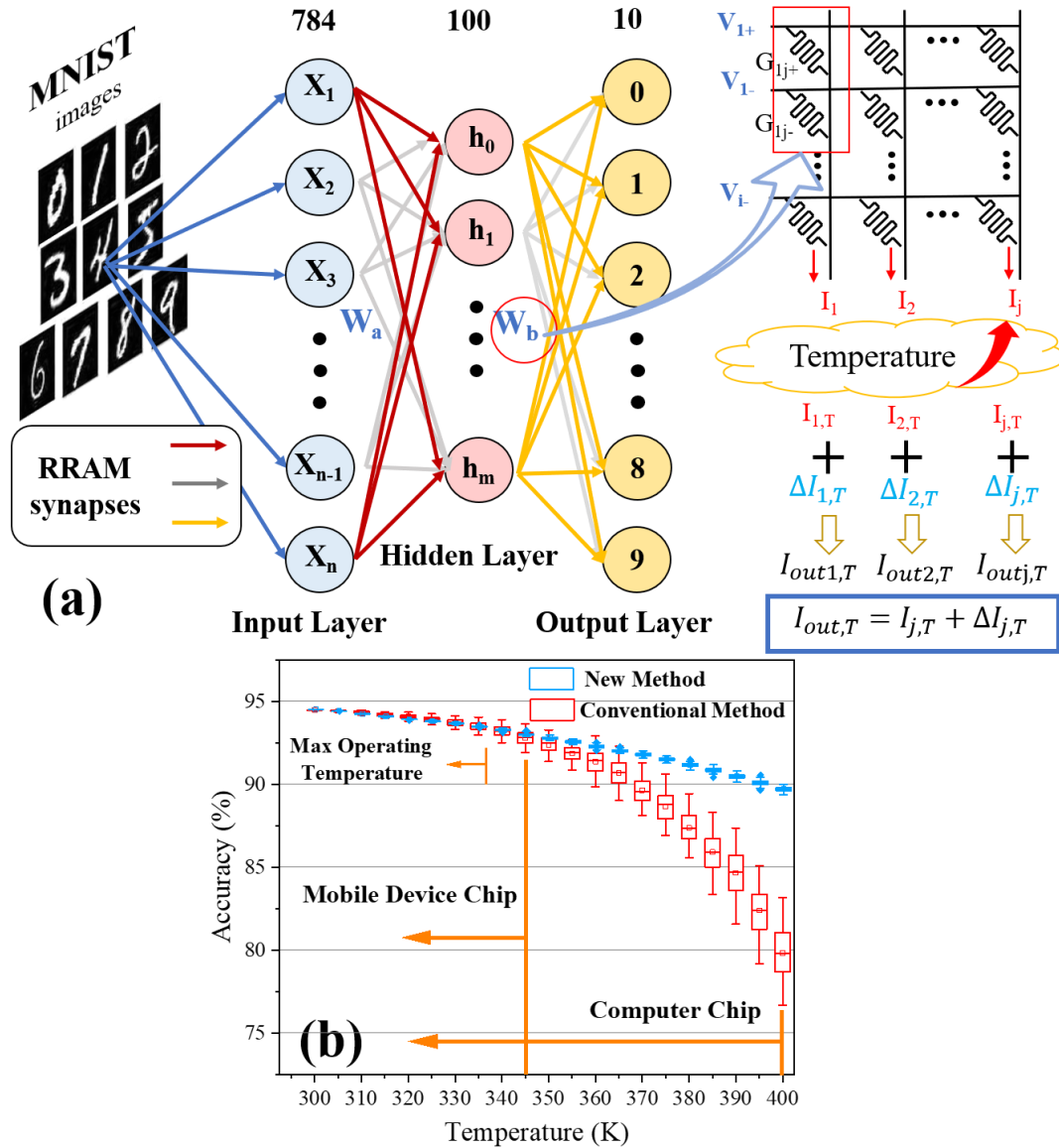


Fig. 5 (a) Schematic of a two-layer fully-connected neural network for recognizing images from the MNIST database, where the weights were implemented with the difference of two conductance in RRAM array. The final output current ($I_{out,j,T}$) at different temperatures can be represented by summing the output current ($I_{j,T}$) of the array and the corresponding compensation current ($\Delta I_{j,T}$). (b) Simulated inference accuracy of 100 RRAM chips as a function of temperature. The maximum operating temperature of the mobile device chip and the computer chip are 340k and 400k, respectively.

In order to display the potential of the compact model to evaluate and optimize neural networks, a standard multi-layer perceptron was used as an example to illustrate the influence of the distribution of T_α in the array on neuromorphic computing systems. This $784 \times 100 \times 10$ fully-connected neural network was used to recognize images from

Modified National Institute of Standards and Technology (MNIST) database on handwritten digits, as shown in Fig. 5(a). The activation functions of the hidden layer and the output layer were rectified linear unit (ReLU)²⁶ and softmax function⁵, respectively. The real-valued weights were linearly mapped to the conductance difference of two RRAM cells, which was composed of the corresponding positive and negative weight rows,

$$I_j = \sum_{i=1}^n G_{ij} \times V_i = \sum_{i=1}^n (G_{ij}^+ - G_{ij}^-) \times V_i \quad (3)$$

where G_{ij} is the conductance of the memory element at array position (i, j). The initial accuracy achieved using software was 97.36% (training with 32-bit single-precision floating-point weights), which was degraded to 94.48% after the quantization using 8-level weights. In order to exclusively investigate T_α impact on neural networks, non-ideal factors such as quantization, circuit parasitic, and retention degradation caused by temperature changes are ignored. The 8-level weight was mapped in the maximum conductance range (12.5 μ S-100 μ S). Generally, the highest operating temperature for mobile device chips is 345K, while the highest temperature for computer chips can reach 400K. When only considering the statistical distribution of T_α , the calculation accuracy with T_α decreased from 94.48% to 79.8% for the mean when the temperature was changed from 300k to 400k.

The existing array programming methods such as write-verify and periodic-refreshing are ineffective in eliminating the impacts of T_α distribution on neuromorphic computing systems because the T_α , as an intrinsic property of a material, is closely related to the device microstructure. Hence, a simple current compensation method is proposed to offset temperature-induced conductance change and recover the network performance. Firstly, a reasonable conductance mapping interval was selected according to the distribution of T_α . The coefficient of variation (c_v) is used to evaluate the dispersion of the T_α distribution in three conductance ranges (high: 50 μ S-100 μ S, middle: 25 μ S-50 μ S, and low: 12.5 μ S-25 μ S),

$$c_v = \frac{\sigma}{\mu} \times 100\% \quad (4)$$

where σ is standard deviation, and μ is mean of T_α . The CV of T_α in the low conductance ranges (5.48%) was less than that in the middle (16.3%) and the high conductance ranges (32.62%). T_α in low conductance ranges were similar, so the cells programmed in such range can be treated as having the same T_α (-0.004K⁻¹). The output current (I_{j,T_0}) of each column at room temperature were store in an integrated non-volatile register. The compensation current value can be calculated by measuring the operating temperature,

$$\Delta I_{j,T} = \sum_{i=1}^n \frac{G_i}{1 + T_\alpha \times \Delta T} \times V_i - \sum_{i=1}^n G_i \cdot V_i = -\frac{T_\alpha \times \Delta T}{1 + T_\alpha \times \Delta T} \times I_{j,T_0} \quad (5)$$

The recovered sum-of-product value ($I_{out,T}$) can be derived by summing actual output current ($I_{j,T}$) and compensation current ($\Delta I_{j,T}$),

$$I_{out,T} = I_{j,T} + \Delta I_{j,T} \quad (6)$$

With the optimized conductance range selection and the current compensation scheme, the accuracy distribution can be maintained at 89.6% for low-side-tail at 400K. However, it is noted that there was no difference between the inference accuracy of the compensation scheme and the initial inference accuracy with a temperature below 350K. The compensation method can reduce more accuracy loss with the temperature from 350K to 400K, but it increased the area and power consumption of the neuromorphic system. The deterioration of the cells retention behavior with increasing temperature will inevitably lead to further accuracy loss. Thus excellent heat dissipation capacity was essential for future applications of neuromorphic computing. Meanwhile, for multi-layer neural networks implemented by analog interfaces, the errors in the front layer accumulate to the next layer²⁷. Compensating the output of the front layer can relieve the inference accuracy loss. More complicated neural network structures also exhibit similar characteristics.

In conclusion, thermal instability based on temperature coefficient(T_α) was comprehensively investigated in the HfO_x-based RRAM array. A compact model was proposed by a 2D atomistic simulation to study the statistical distribution of T_α on the array level. Based on the simulation of the SET process and perturbation process of the RRAM cells in the array, the physical mechanism of instability of cells with positive T_α was elucidated. A compensation scheme was proposed in this letter by selecting the appropriate conductance range for the weight-conductance mapping and adding compensation current, which can effectively recover the inference accuracy. With this scheme, the mean MNIST inference accuracy of a multi-layer neural network can be improved remarkably. Our results are crucial for the evaluation and optimization of RRAM-based neuromorphic computing systems.

ACKNOWLEDGMENT

We thank Laboratory of Emerging Memory and Novel Computing of Tsinghua University for providing HfO_x-based 1kbit RRAM array for testing. We acknowledge the financial support by the National Natural Science Foundation of China (Grant Nos. 61804105) and the Fundamental Research Funds for the Central Universities (Grant No. DUT19RC(3)029).

DATA AVAILABILITY

The data that support the findings of this study are available from the corresponding authors upon reasonable request.

REFERENCES

- ¹ A. Sebastian, M. Le Gallo, R. Khaddam-Aljameh, and E. Eleftheriou, *Nature Nanotechnology* **15**, 529 (2020).
- ² H. Lu, Y. Li, M. Chen, H. Kim, and S. Serikawa, *Mobile Netw Appl* **23**, 368 (2018).
- ³ W. Zhang, B. Gao, J. Tang, P. Yao, S. Yu, M.-F. Chang, H.-J. Yoo, H. Qian, and H. Wu, *Nat Electron* **3**, 371 (2020).
- ⁴ M.A. Zidan, J.P. Strachan, and W.D. Lu, *Nature Electronics* **1**, 22 (2018).
- ⁵ F. Cai, J.M. Correll, S.H. Lee, Y. Lim, V. Bothra, Z. Zhang, M.P. Flynn, and W.D. Lu, *Nature Electronics* **2**, 290 (2019).
- ⁶ C. Li, M. Hu, Y. Li, H. Jiang, N. Ge, E. Montgomery, J. Zhang, W. Song, N. Dávila, C.E. Graves, Z. Li, J.P. Strachan, P. Lin, Z. Wang, M. Barnell, Q. Wu, R.S. Williams, J.J. Yang, and Q. Xia, *Nature Electronics* **1**, 52 (2018).
- ⁷ W. Zhang, **3**, 12 (2020).
- ⁸ P. Yao, H. Wu, B. Gao, J. Tang, Q. Zhang, W. Zhang, J.J. Yang, and H. Qian, *Nature* **577**, 641 (2020).
- ⁹ Q. Liu, B. Gao, P. Yao, D. Wu, J. Chen, Y. Pang, W. Zhang, Y. Liao, C.-X. Xue, W.-H. Chen, J. Tang, Y. Wang, M.-F. Chang, H. Qian, and H. Wu, in *2020 IEEE International Solid-State Circuits Conference - (ISSCC)* (IEEE, San Francisco, CA, USA, 2020), pp. 500–502.
- ¹⁰ M. Zhao, B. Gao, J. Tang, H. Qian, and H. Wu, *Applied Physics Reviews* **7**, 011301 (2020).
- ¹¹ M. Zhao, H. Wu, B. Gao, Q. Zhang, W. Wu, S. Wang, Y. Xi, D. Wu, N. Deng, S. Yu, H.-Y. Chen, and H. Qian, in *2017 IEEE International Electron Devices Meeting (IEDM)* (IEEE, San Francisco, CA, USA, 2017), p. 39.4.1-39.4.4.
- ¹² P. Huang, Y.C. Xiang, Y.D. Zhao, C. Liu, B. Gao, H.Q. Wu, H. Qian, X.Y. Liu, and J.F. Kang, in *2018 IEEE International Electron Devices Meeting (IEDM)* (IEEE, San Francisco, CA, 2018), p. 40.4.1-40.4.4.
- ¹³ P.-Y. Chen, X. Peng, and S. Yu, in *2017 IEEE International Electron Devices Meeting (IEDM)* (IEEE, San Francisco, CA, USA, 2017), p. 6.1.1-6.1.4.
- ¹⁴ M. Zhao, H. Wu, B. Gao, X. Sun, Y. Liu, P. Yao, Y. Xi, X. Li, Q. Zhang, K. Wang, S. Yu, and H. Qian, in *2018 IEEE International Electron Devices Meeting (IEDM)* (IEEE, San Francisco, CA, 2018), p. 20.2.1-20.2.4.
- ¹⁵ Y. Lin, C. Wang, M. Lee, D. Lee, Y. Lin, F. Lee, H. Lung, K. Wang, T. Tseng, and C. Lu, *IEEE Transactions on Electron Devices* **66**, 1289 (2019).
- ¹⁶ R. Fang, W. Chen, L. Gao, W. Yu, and S. Yu, *IEEE Electron Device Lett.* **36**, 567 (2015).
- ¹⁷ F.M. Puglisi, A. Qafa, and P. Pavan, *IEEE Electron Device Lett.* **36**, 244 (2015).
- ¹⁸ T. Schultz and R. Jha, in *2019 IEEE 62nd International Midwest Symposium on Circuits and Systems (MWSCAS)* (IEEE, Dallas, TX, USA, 2019), pp. 464–467.
- ¹⁹ L. Wang, A.V.-Y. Thean, and G. Liang, *Appl. Phys. Lett.* **112**, 253505 (2018).
- ²⁰ X.H. Wang, H. Wu, B. Gao, X. Li, N. Deng, and H. Qian, *IEEE Electron Device Lett.* **39**, 192 (2018).

- ²¹ U. Russo, D. Ielmini, C. Cagli, A.L. Lacaita, S. Spiga, C. Wiemer, M. Perego, and M. Fanciulli, in *2007 IEEE International Electron Devices Meeting (2007)*, pp. 775–778.
- ²² T.P. Xiao, C.H. Bennett, B. Feinberg, S. Agarwal, and M.J. Marinella, *Applied Physics Reviews* **7**, 031301 (2020).
- ²³ B. Gao, H. Wu, W. Wu, X. Wang, P. Yao, Y. Xi, W. Zhang, N. Deng, P. Huang, X. Liu, J. Kang, H.-Y. Chen, S. Yu, and H. Qian, in *2017 IEEE International Electron Devices Meeting (IEDM)* (IEEE, San Francisco, CA, USA, 2017), p. 4.4.1-4.4.4.
- ²⁴ W. Guan, M. Liu, S. Long, Q. Liu, and W. Wang, *Appl. Phys. Lett.* **93**, 223506 (2008).
- ²⁵ W. Wu, H. Wu, B. Gao, N. Deng, S. Yu, and H. Qian, *IEEE Electron Device Lett.* **38**, 1019 (2017).
- ²⁶ C.-C. Chang, J.-C. Liu, Y.-L. Shen, T. Chou, P.-C. Chen, I.-T. Wang, C.-C. Su, M.-H. Wu, B. Hudec, C.-C. Chang, C.-M. Tsai, T.-S. Chang, H.-S.P. Wong, and T.-H. Hou, in *2017 IEEE International Electron Devices Meeting (IEDM)* (2017), p. 11.6.1-11.6.4.
- ²⁷ M. Hu, J.P. Strachan, Z. Li, E.M. Grafals, N. Davila, C. Graves, S. Lam, N. Ge, J.J. Yang, and R.S. Williams, in *Proceedings of the 53rd Annual Design Automation Conference* (ACM, Austin Texas, 2016), pp. 1–6.